Energy Conversion and Management 291 (2023) 117298

Contents lists available at ScienceDirect

Energy Conversion and Management

journal homepage: www.elsevier.com/locate/enconman

A multi-objective optimisation framework to design membrane-based energy recovery ventilation for low carbon buildings

Peng Liu [a,*], Hans Martin Mathisen [b], Maria Justo Alonso [a], Anneli Halfvardsson [c]

[a] Department of Architecture, Materials and Structures, SINTEF Community, Trondheim, Norway
[b] Department of Energy and Process Engineering, Norwegian University of Science and Technology, Trondheim, Norway
[c] Department of Research & Technology, Flexit AS, Ørje, Norway

ARTICLE INFO

Keywords:
Multi-objective optimisation
Membrane energy exchanger
Energy-efficient ventilation

ABSTRACT

Membrane energy exchangers (MEEs) are increasingly being studied and utilized to contribute to realising energy-efficient building services and providing satisfactory indoor environments. The performance of MEEs has been extensively studied in terms of heat and mass transfer and pressure drop (PD). However, a model for optimizing the performance of membrane energy exchangers in residential ventilation, which takes into account the influential factors, is lacking in order to support the design of membrane energy exchangers. The purpose of this study was to establish a framework for the multi-objective optimisation design of membrane energy exchanger performance. This framework was demonstrated by considering the competing objectives of maximising thermal recovery effectiveness and minimising pressure drop. One of the constraints used for optimising membrane energy exchangers was the total membrane area, which strongly influences the investment cost of the exchanger. Another constraint was the moisture recovery intensity of the membrane energy exchangers, which affects indoor humidity levels. Pareto optimal solutions were obtained by solving the developed multi-objective optimisation framework using the genetic algorithm in MATLAB.

Using multi-objective optimisation, the pressure drop of the MEE was reduced by 41% while the thermal recovery effectiveness remained unchanged. The resulting pressure drops as low as 5 Pa, enables the application of membrane energy exchangers in natural and hybrid ventilation. Factors influencing the Pareto optimal solutions including moisture recovery effectiveness, total membrane area and operating airflows have been investigated. A better understanding of optimal membrane energy exchanger designs considering thermal recovered energy and fan power resulted from this study.

1. Introduction

The building sector is responsible for approximately 32% of the global energy consumption (24% residential and 8% commercial) [1] and 30% of total carbon dioxide (CO_2) emissions [2]. Heating, ventilation and air conditioning (HVAC) systems are essential for ensuring a healthy and comfortable indoor environment but are recognized as major energy consumers in commercial and residential buildings [3]. The energy demands of HVAC systems are increasing and will continue to rise contemporaneously with global population growth, expanding urbanisation and economic activity, and corresponding increases in requirements for improved indoor thermal comfort [4]. Thus, achieving energy-efficient HVAC systems is crucial to realising zero-energy and zero-emissions buildings [5].

Heat recovery systems (HRS) encompass equipment designed to enable the recovery of a portion of the energy available from conditioned indoor air through a mechanical ventilation system. Heat recovery technology has the capacity to recuperate up to 90% of ventilation heat losses [6]. Membrane energy exchangers (MEEs) have been recognised as essential component for the next generation of HVAC systems [7]. Their use in both hot and cold climates has demonstrated significant energy savings due to significantly reduced energy demands for humidification, dehumidification, and frost control. [8]. For example, in hot and humid regions of Hong Kong, MEEs have been reported to as saving about 58% of the energy required for annual air conditioning due to the mitigated energy use of dehumidification resulting from the moisture transfer feature of the MEE [9]. By comparison, conventional sensible-only heat recovery can save only 10% [9]. In cold climates, the application of MEEs was initialised by the frost

* Corresponding author.
E-mail address: peng.liu@sintef.no (P. Liu).

https://doi.org/10.1016/j.enconman.2023.117298
Received 24 March 2023; Received in revised form 5 June 2023; Accepted 10 June 2023
Available online 14 June 2023

Nomenclature

Parameters

a	Half width of the air channel (m)
b	Half height of the air channel (m)
A	Heat and mass transfer area (m^2)
c_p	Specific heat of air ($J/kg \bullet K$)
D_h	Hydraulic diameter of air channel (m)
D_v	Diffusivity (m^2/s)
f	Friction factor
F	Objective function
g_c	Proportionality constant, $g_c = 1$
h	Convective heat transfer coefficient ($W/m^2 \bullet K$)
k	Convective mass transfer coefficient (m/s)
L	Length (m)
Le	Lewis number
$\dot{m}$	Mass flow rate of ventilation air (kg/s)
NTU	Number of transfer unit
Nu	Nusselt number
r	Mass transfer resistance through membrane (m^2s/kg)
Sh	Sherwood number
U	Overall heat transfer coefficient ($W/m^2 \bullet K$) or uncertainty
X	Decision variable
Y	Function

Greek letters

ε	Effectiveness
δ	Membrane thickness (m)
λ	Thermal conductivity [$W/(m \bullet K)$]
α^*	Aspect ratio
Δp	Pressure drop (Pa)

Subscripts

a	Air
e	Exhaust
l	Latent
m	Membrane
min	Minimum
s	Supply
spec	Specific
tot	Total

Abbreviations

AHU	Air handling unit
MEE	Membrane energy exchanger
PD	Pressure drop (Pa)
RH	Relative humidity (%)
MRE	Moisture recovery effectiveness (%)
TRE	Thermal recovery effectiveness (%)

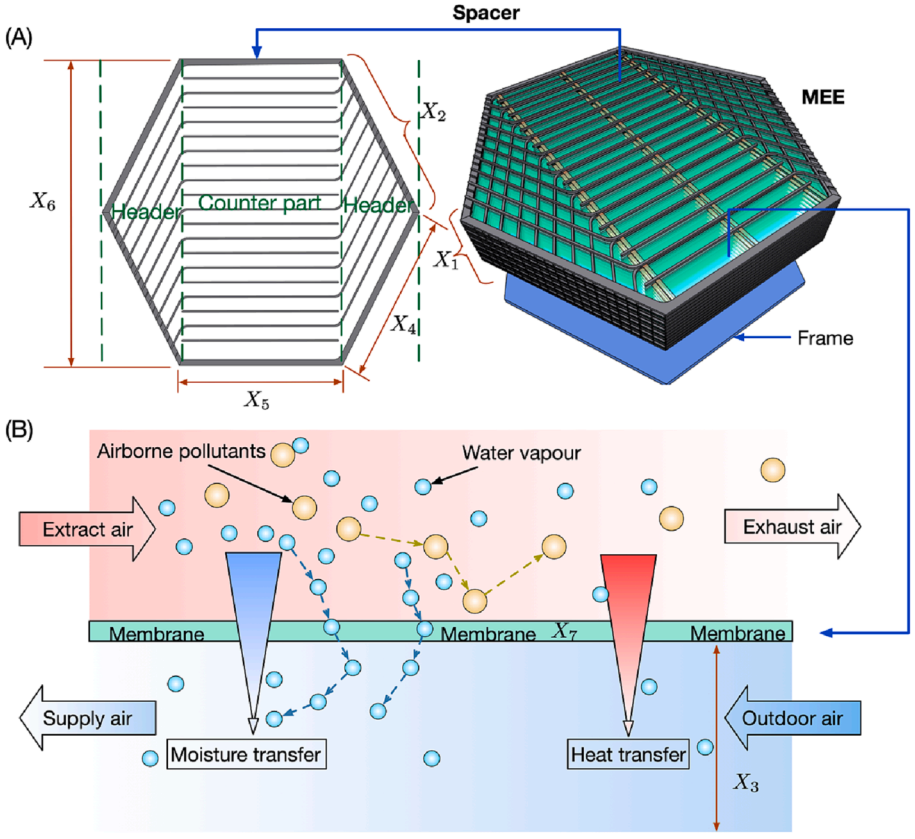

Fig. 1. Schematic showing: (A) quasi-counterflow MEE and spacer; and (B) heat and mass transfer mechanism through a membrane (adapted from [13]).

problem inside the heat recoveries [10]. MEEs can reduce or even avoid the built-up frost as the moisture transfer from the moist extract air to the supply air can lower the dew point of the exhaust air [11].

MEEs enable both heat and moisture transfer by utilising semi-permeable membranes, as illustrated in Fig. 1. In principle, these membranes are supposed to inhibit airborne pollutants and odour

transfer, and thus reduce cross-contamination risk [12], as illustrated in Fig. 1. The odour transfer through a porous membrane have been experimentally investigated [13]. According to this study [13], odours generated in kitchens and bathrooms are likely to be transferred undesirably to supply air through the tested polypropylene membrane exchanger. Extensive studies have recently been performed on air-to-air MEEs that have shown they have advantageous features, such as their compact construction, absence of moving parts, ease of maintenance and cleaning [7], their low cost, high recovery effectiveness [14], and their ability to recover heat and moisture [15], which has enabled the improvement of dry indoor air [16] and their great potential for reducing frost risk inside the exchanger [17].

Quasi-counterflow MEEs with counterflow core parts and headers (Fig. 1(A)) can recover around 80–95% of the heat from the extract air as a result of the counterflow arrangement [18]. The headers of the quasi-counterflow MEE allow ease of connection to the ductwork, compared to the pure counterflow arrangement. Zhang [19] mathematically modelled and experimentally verified a quasi-counter flow MEE concluding that the thermal recovery effectiveness (TRE) and moisture recovery effectiveness (MRE) of the constructed quasi-counterflow MEE lies between those for cross-flow and pure counterflow [19]. Kays and London [20] showed that the TRE and MRE of quasi-counterflow can be calculated by combining the number of transfer units for the header part and those for the pure counterflow part. Al-Waked et al. [21] investigated the thermal performance enhancement of MEE under turbulent flow regimes using the computational fluid dynamics (CFD) approach. Their study found that face velocity has a greater impact on thermal performance than the channel spacer. The quasi-counterflow layout may provide a superior overall option to the L-shape flow layout [21]. Asasian-Kolur et al. [22] investigated all the aspects that affect the non-isothermal performance of MEEs. In their study, the development of MEEs, heat and moisture transfer mechanisms across different membranes were studied.

A considerable number of studies have focused on the enhancement of heat and moisture transfer in quasi-counterflow MEEs through the improvement of the MEE structure, and advances in membranes and airflow arrangements. Zhang [15] determined that MEEs could provide energy-efficient air conditioning in hot and humid climates through a substantial reduction in the need to cool and dehumidify the fresh air. Liu et al. [14] demonstrated the potential of quasi-counterflow MEEs in reducing the frost risk resulting from moisture recovery in cold climates, as compared to the sensible-heat-only plate exchangers [18]. The quasi-counterflow MEE tested by Liu et al. [14] exhibited high sensible effectiveness (over 90%) and high latent (above 80%) effectiveness. However, the pressure drop (PD) through the MEE developed with mesh spacers [14] was relatively high, which may limit its practical applications.

Previous research has established that a high moisture recovery effectiveness (MRE) can lower the frost formation risk inside MEEs [23]. Recovered moisture can also humidify the dry indoor air in cold climates, as discussed by Liu et al. [24]. However, high MRE may lead to issues, such as condensation on the interior surface of buildings and mould growth. Thus, an optimal moisture recovery intensity exists, and it should be considered as a constraint on optimising MEEs [16]. The methods established by Liu et al. [16] can be used to determine optimal moisture recovery intensity.

Spacers are typically needed in MEEs to reinforce and support the thin flexible membranes. Various spacers have been examined for their use in MEEs, such as those in Koester et al [25], and Woods and Kozubal [26]. Spacers cause an additional PD due to frictional resistance through the confined channel constituted by the membrane and spacers. The air needs to be pumped through the MEE, which requires more fan power. As a result, PDs directly impact electricity use and peak power demands [27]. When designing heat recovery systems, PD may conflict with thermal energy recovery. In a measurement study of 13 ventilation systems in Switzerland, Roulet et al. [28] identified three systems that saved little or even consumed more energy, as part of the heat recovery due to PD, parasitic shortcuts, leakage and other malfunctions. Further research is required regarding the trade-off between heat recovery and PD in MEE design.

According to Mariana and Riffat [18], the heat and mass transfer in MEEs are primarily affected by the membrane materials and airflow arrangements. Future optimisation studies should concentrate on the physical and performance parameters of the MEE. A recent review on progress and advances in air-to-air MEEs [7] pointed out that limited effort has been spent on MEE performance-based design optimisation. Thermal energy recovery and PD are conflicting factors, therefore optimising one factor with respect to a single objective can result in unacceptable results concerning the other factor.

There are two general ways to deal with multi-objective optimisation problems. One is to integrate all the objectives into one single composite objective function and the other is to move all but one objective as constraints [29]. The single-objective approach requires methods, such as utility theory or the weighted sum method, to combine all the objectives [29]. However, it is difficult to determine the correct weights or unity functions to describe and reflect the decision-maker's preferences.

The other optimisation approach is to determine a series of optimal solutions, each of which fulfils the objectives without being dominated by any other solution [29]. A set of optimal solutions is developed, referred to as a Pareto front, which can reflect the trade-offs between objectives.

Energy in the forms of electricity (indicating the PD) and thermal energy displays differences in quality concerning different energy mixes and at different times [20]. Combining these two factors into one single objective function may lead to unfavourable optimisation results and thus misled decision-making. The method with a set of optimal solutions with multi-objective optimisation can tackle conflicting objectives, allowing both recovery effectiveness and pressure drop to be taken into account. Despite the importance of optimising the performance of MEE in terms of recovered thermal energy and fan power requirements, the multi-objective optimisation of MEE remains under-explored. Further research is required to gain a systematic understanding of how different factors influence the optimisation results.

The current study developed a multi-objective optimisation framework for MEEs that provided a set of Pareto optimal solutions including a combination of TRE and PD. The total membrane area—potentially the most expensive dimension—and the influence of the MRE on the indoor humidity were constraints. The major contributions and novelties of this study are as follows.

1. A genetic algorithm (GA) multi-objective optimisation framework was established to improve the MEE design and support decision-making with respect to TRE and PD.
2. The effect of moisture recovery resulting from the permeable membranes on indoor humidity levels was considered one constraint in the course of the optimisation. To our knowledge, the comprehensive consideration of moisture recovery concerning MEE structure and membrane properties, and their impacts on indoor humidity in optimisation, have not been reported previously.
3. The provision of a basis for an MEE techno-economics assessment through the presentation of the optimisation results for various maximum total membrane areas. The consideration of moisture recovery thresholds in the optimisation may contribute to growing MEE applications.

2. Materials and methods

The models of heat and mass transfer and PD for the quasi-counterflow MEE are described in this section. The models presented were sequentially used for optimisation by changing the design input parameters in their eligible ranges. This study applied the multi-objective optimisation approach with the aim of maximising the heat

Table 1
Design parameters for the initial design of the quasi-counterflow MEE.

Design parameter	Value for verified MEE (initial design)	Unit
Number of layers (X_1)	48	—
Number of channels for each layer (X_2)	10	—
Channel height (X_3)	2	mm
Side length of inlet/outlet (X_4)	200	mm
Length of counterflow core part (X_5)	190	mm
Width of counterflow core part (X_6)	357	mm
WV transfer resistance (X_7)	78	s/m

recovery effectiveness and minimising the PD for the MEEs. The channel aspect ratio, total membrane area and MRE were defined as constraints in the multi-objective optimisation process.

2.1. Sensible and latent effectiveness models of membrane energy exchanger and the pressure drop model

This study used the quasi-counterflow MEE illustrated in Fig. 1 as the initial design. The dimensions and geometry of the MEE for the initial design are specified in Table 1. However, the values of the initial design parameters were changed within defined eligible ranges in order to obtain optimal designs. Decision variables in optimisation are illustrated as X1–X7 in Fig. 1, which correspond to the design parameters used in this study. Analytical models for the MEE concerning heat and moisture transfer and PD were developed concurrently with the change of design parameters in the multi-objective optimisation.

The quasi-counterflow MEE was analytically modelled and divided into three parts—two header parts and a counterflow part, as depicted in Fig. 2.

2.1.1. Thermal recovery effectiveness model

The effectiveness-number of transfer units (ε-NTU) method [20] was applied to determine the TRE (also known as the sensible effectiveness) of the MEE. The analytical forms of TRE for different flow arrangements have been described by Shah and Sekulic [27]. For the quasi-counterflow arrangement, the overall effectiveness of the heat exchanger was obtained by combining the cross-flow header part and counterflow core part, as detailed by Kays and London [20]. In optimisations with varying geometries and dimensions (Fig. 2), the flow arrangements in the header parts can vary from near-counterflow ($\alpha \approx 180^{\circ}$), to cross-flow ($\alpha = 90^{\circ}$) and near-concurrent flow ($\alpha \approx 0^{\circ}$) by changing the angle (α). For this study, the TRE of the header part was determined by an interpolation approach. The dimensions of the counterflow part in Fig. 2 also changed within the eligible searching range during the optimisation.

The TRE of the counterflow arrangement for the counterflow header and counterflow part of the MEE ($\alpha = 180^{\circ}$ in Fig. 2) can be calculated as

$$TRE_{\text{counter}} = \frac{NTU_{\text{counter}}}{1 + NTU_{\text{counter}}} \tag{1}$$

For the cross-flow arrangement, the TRE of the header ($\alpha = 90^{\circ}$ in Fig. 2) is

$$TRE_{\text{cross}} = 1 - \exp\left[\frac{\exp\left(-NTU_{cross}^{0.78}\right) - 1}{NTU_{cross}^{-0.22}}\right] \tag{2}$$

The TRE of the parallel header part ($\alpha = 0^{\circ}$ in Fig. 2) is

$$TRE_{\text{parallel}} = \frac{1}{2}\left[1 - \exp\left(-NTU_{\text{parallel}}\right)\right] \tag{3}$$

Determination of the NTUs for MEEs has been addressed by Liu et al. [30], and Niu and Zhang [31]. The essential equations used to calculate the NTUs are given below.

The number of heat transfer units is defined as

$$NTU_s = \frac{U_s A}{(\dot{m}C_{\text{P}})_{min}} \tag{4}$$

The numerator in Eq. (4), which is the overall heat transfer coefficient multiplied by the total heat transfer area, can be calculated by

$$U_s A = \left(\frac{1}{h_s A_s} + \frac{\delta}{\lambda_m A_m} + \frac{1}{h_e A_e}\right)^{-1} \tag{5}$$

In Eq. (5), the middle term, $\frac{\delta}{\lambda_m A_m}$, which represents the heat conduction resistance through the membranes, can be neglected due to the membranes being thin. In Eq. (5), $\frac{1}{h_s A_s}$ and $\frac{1}{h_e A_e}$ represent the convective heat transfer resistance on the supply and exhaust sides, respectively.

The convective heat transfer coefficient, h, is calculated by

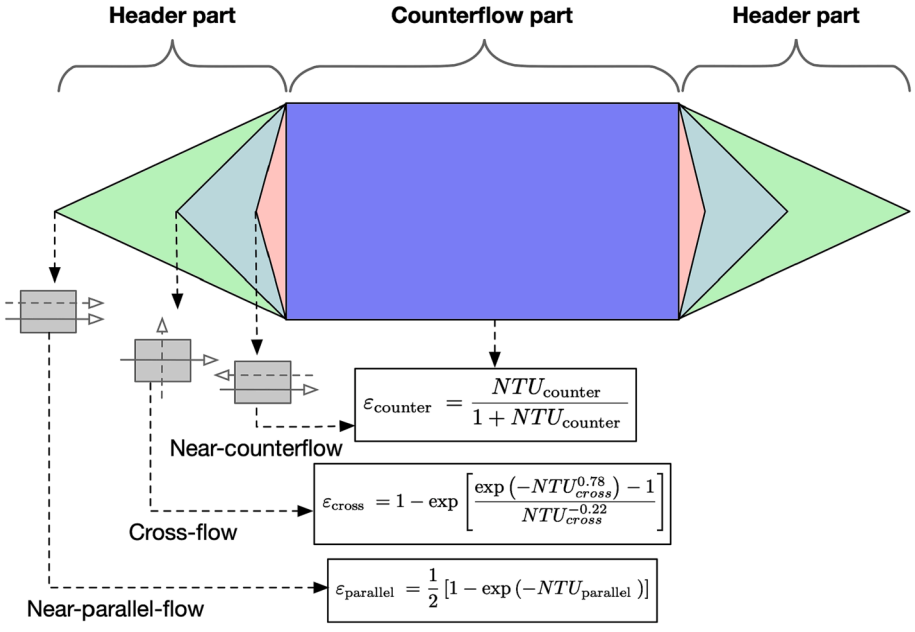

Fig. 2. Quasi-counterflow MEE, showing counterflow core part and headers with various flow arrangements.

$$h = \frac{Nu\lambda_a}{D_h} \tag{6}$$

where λ_a is the thermal conductivity of the air, which is a constant in the defined eligible range of this study. The hydraulic diameter, D_h, is

$$D_h = \frac{4ab}{a+b} \tag{7}$$

where 2a is the width of the rectangular channel and 2b is the height of the rectangular channel.

The Nusselt number, *Nu*, was determined for the fully developed laminar flow in the rectangular channel. The boundary condition of constant heat flux rate was used in this study because it is commonly applied in counterflow heat exchangers. The Nusselt number varied with the different aspect ratios of the rectangular channels. The analytical correlation of the Nusselt number (*Nu*) is given in Eq. (8) [32].

$$Nu = 8.235\left(1 - 2.0421\alpha^* + 3.0853\alpha^{*2} - 2.4765\alpha^{*3} + 1.0578\alpha^{*4} - 0.1861\alpha^{*5}\right) \tag{8}$$

The aspect ratio (α^*) of the rectangular duct in the MEE is the ratio of the channel height (2b) to the channel width (2a).

2.1.2. Moisture recovery effectiveness model

The MRE can be calculated using a similar procedure to that for the TRE calculation using the heat and mass transfer analogy for quasi-counterflow MEEs [19]. Employing the Chilton–Colburn analogy [32], the Sherwood number, *Sh*, which reflects the convective moisture transfer, is expressed as

$$Sh = NuLe^{-1/3} \tag{9}$$

where *Le* is the Lewis number and is assumed to be a constant of 1.2 for the ventilation air and WV mixture in this study. The Nusselt number, *Nu*, was determined using Eq. (8) for a fully developed rectangular duct channel.

As with the convective heat transfer coefficient, *h*, the convective moisture transfer coefficient, *k*, can be calculated by

$$k = \frac{ShD_v}{D_h} \tag{10}$$

where D_v is the WV diffusivity in air, which was a constant of $2.42*10^{-5}$ m^2/s in this study.

The number of the moisture transfer unit, NTU_l, is

$$NTU_l = \frac{U_l A}{\dot{m}_{min}} \tag{11}$$

Similarly, the overall moisture transfer coefficient can be calculated by

$$U_l A = \left(\frac{1}{k_s A_s} + \frac{r_{mm}}{A_m} + \frac{1}{k_e A_e}\right)^{-1} \tag{12}$$

Unlike in Eq. (5), the diffusion term $\frac{r_{mm}}{A_m}$ cannot be neglected in Eq. (12) because it can account for 60–90% of the total moisture transfer resistance, as estimated by Min and Su [33]. The diffusive resistance varies with different (dense or porous) membrane types, membrane properties (WV permeability) and membrane thickness.

Eqs. (1)–(3) can be applied to calculate the MRE for different airflow arrangements when the number of heat transfer units is substituted by the number of moisture transfer units, NTU_l. The overall MRE can also be obtained by combining the header and counterflow parts through chain-rule methodology [34].

2.1.3. Pressure drop model through the quasi-counterflow membrane energy exchanger

One of the flow channels in the quasi-counterflow MEE is shown in Fig. 3, which also shows the airflow and the static pressure variation in the flow direction. The incoming airflow to the channel (0 → 1 in Fig. 3) is assumed to be uniform. As it enters the channel, the static pressure drops (1 → 2) due to the contraction of the free-flow area. In the core, the PD is caused both by skin friction (2 → b, c → d and e → 3) and the change in the flow direction (b → c and d → e). At the entrance to channel (2 → a), the static pressure decreases more sharply due to the entrance effect of the developing velocity profile. After the airflow exits the channel, a pressure rise (3 → 4) occurs due to the expansion of the free-flow area. The total PD through the MEE is equal to the PD for one single channel because they are in parallel, as calculated by

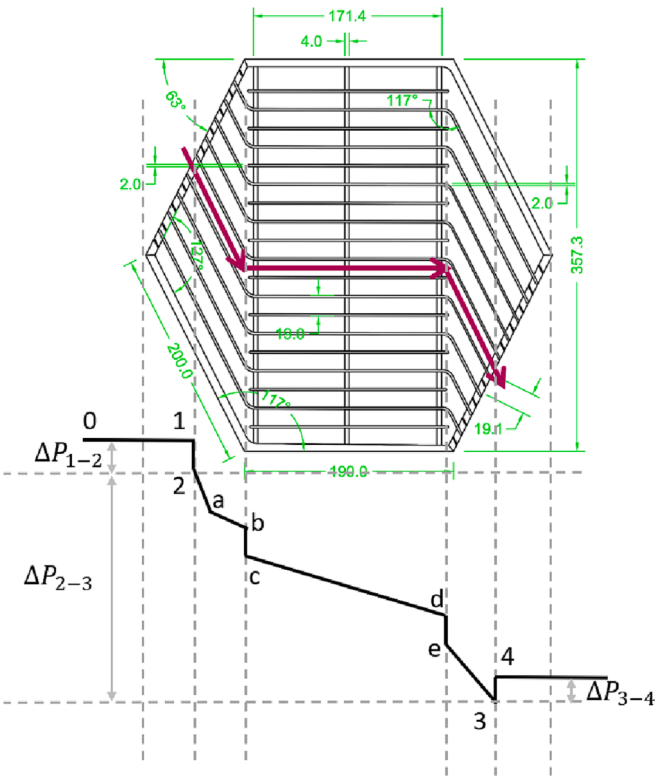

Fig. 3. Static pressure changes and airflow direction through one quasi-counterflow MEE channel for the initial MEE dimension (pressure changes not to scale).

$$PD = \Delta p_{1-2} + \Delta p_{2-3} - \Delta p_{3-4} \tag{13}$$

where subscripts 1–4 represent locations in the core of the MEE. Δp_{1-2}, Δp_{2-3} and Δp_{3-4} are denoted in Fig. 3, Δp_{1-2} being the PD at the core entrance resulting from the sudden contraction of the free-flow area, Δp_{2-3} is the core PD, including the frictional pressure loss and a local loss due to changes in the flow direction, and Δp_{3-4} is the pressure rise at the core exit resulting from the sudden expansion of the free-flow area. The core pressure loss (Δp_{2-3}) is the dominant term, accounting for more than 90% of the total PD for airflow [35]. The pressure loss (Δp_{1-2}) and the pressure rise (Δp_{3-4}) generally compensate for each other. Thus, only the core PD (Δp_{2-3}) is calculated and summed for different frictional elements. The generic form of the PD calculation is [27]

$$PD \approx \left(f\frac{L}{D_h} + \sum K\right)\frac{V^2}{2g_c} \tag{14}$$

The friction factor, *f*, which was experimentally derived from Shah and Sekulic [27] for the different aspect ratios of the rectangular channel for a laminar flow and changes in the flow direction, was applied when the MEE design parameters were changed when seeking optimal designs in this study. *K* is a pressure loss coefficient that accounts for local pressure loss due to changes in the flow direction between the headers and the counterflow part.

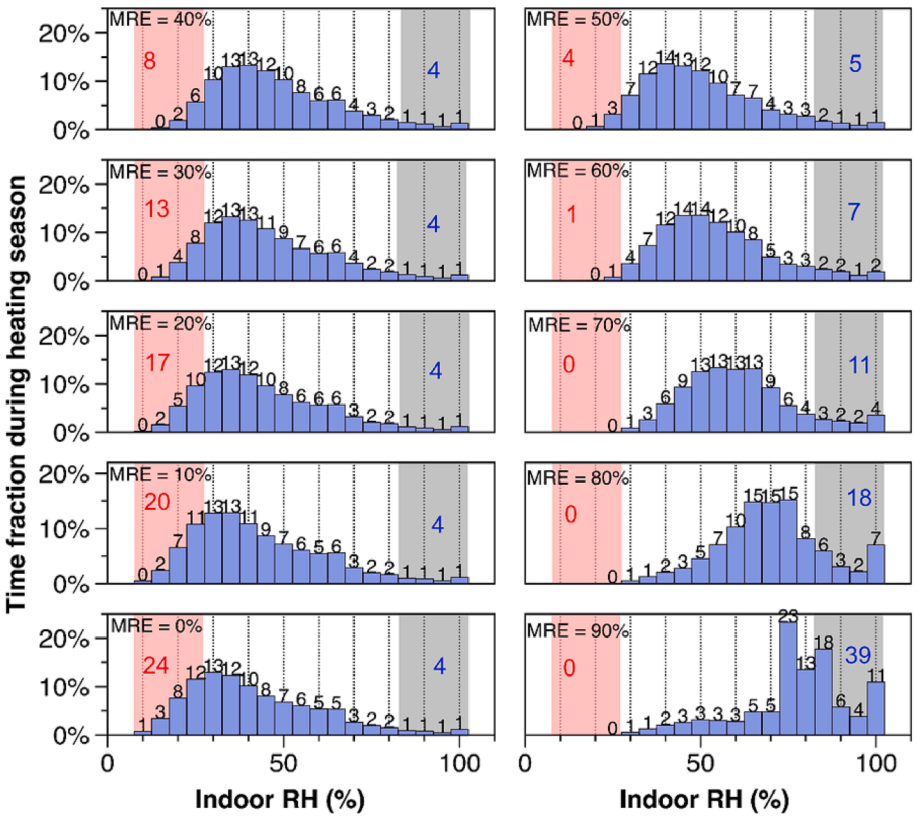

Fig. 4. Time fractions of indoor relative humidity (RH) levels for various latent effectiveness in all rooms during the heating season (November to March) [16]. Red shading—too-dry air below 20%, red values—time fraction of dry air, grey shading—too-humid air with RH over 80%, blue values—the sum of time fractions of too-humid air.

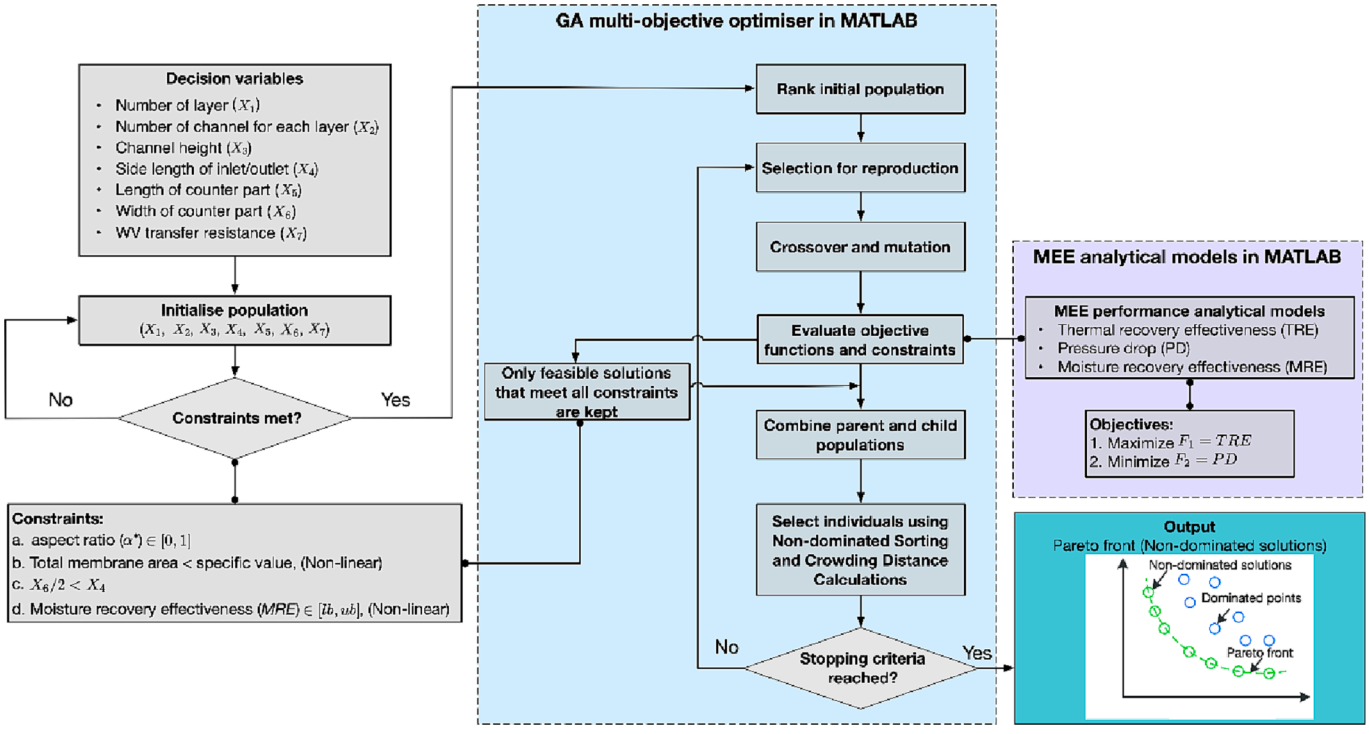

Fig. 5. Workflow showing a multi-objective optimisation framework for providing optimal MEE designs.

2.2. Moisture recovery effectiveness threshold for healthy indoor humidity levels

Indoor air humidity is affected by sources of moisture generation (e.g. the presence and activities of humans), ventilation, moisture recovery, the hygroscopic surfaces of the envelope and furniture, condensation, and outdoor air humidity. As all of these factors are interconnected, the moisture recovery influence of MEEs on indoor humidity levels is not obvious. A recent analytical study [16] revealed the optimal MRE (referred to as 'latent effectiveness' in this study) by considering the lowest operation time falling outside of the defined extreme indoor relative humidity (RH) (<20% or greater than 80%). The verified analytical results were illustrated for a single-family house in Oslo, Norway [16]. The major determination process is explained in Fig. 4 [16]. It was found that the optimal moisture recovery was within a range of 50–60% for the given conditions [16], with the too-dry conditions being dramatically reduced and the too-humid situations not being significantly increased. In the current study, an MRE in a range of 50–60% was used as a nonlinear constraint for the multi-objective optimisation. The determination of the MRE (latent effectiveness) is given in Section 2.1.2. Employing the methods presented by Liu et al. [16], different MREs (latent effectiveness) that were best adapted to different indoor moisture sources and climates could be applied as the constraint for multi-objective optimisation.

2.3. Multi-objective optimisation method

In this section, the multi-objective optimisation framework is presented for optimising the thermal recovery performance of MEEs and the PD through the MEEs considering the total membrane area and the effect of moisture recovery on the indoor humidity.

The goal of multi-objective optimisation is to minimise or maximise multiple objective functions while subjecting them to a set of constraints. Pareto fronts are sets of points in a decision variable space that do not have inferior fitness function values. Therefore, one fitness function can only be improved by deteriorating another on the Pareto front. The genetic algorithm (GA) [36] is probably the most commonly utilised technique for determining the Pareto front for multi-objective optimisation problems. The GA employs a genetic search procedure based on the basic elements of natural genetics, including reproduction, crossover, and mutation.

The GA solver (gamultiobj) in MATLAB [37] was used to find the Pareto front for the multi-objective optimisation problem in this work. The GA solver is a variant of NSGA-II [38] and employs a controlled, elitist genetic algorithm [37]. An elitist GA always rewards individuals with a better fitness value (rank). Additionally, a controlled elitist GA favours individuals that are capable of increasing the diversity of the population as a whole, even if their fitness value is lower [37]. Maintaining a diversity of population is essential for convergence to an optimal Pareto front. A more detailed explanation of GA can be found in MATLAB help [37].

The optimisation process was carried out following the workflow of the multi-objective optimisation design framework schematically illustrated in Fig. 5. The multi-objective optimisation problem for this work was formulated as follows.

Objectives:

1. $\max(F_1 = TRE)$
2. $\min(F_2 = PD)$

Subject to:

a. $0 < \alpha^* < 1$
b. $A_{tot} \leq A_{spec}$
c. $X_6/2 < X_4$ (the hypotenuse of a triangle is larger than the right-angle side)

Table 2
Decision-variable thresholds and verified design values used in this study.

Type	Decision variable	Threshold	Verified MEE value (initial design)	Unit
Integer	Number of layers (X_1)	[10,200]	48	—
Integer	Number of channels for each layer (X_2)	[10,20]	10	—
Continuous	Channel height (X_3)	[2,10]	2	mm
Continuous	Side length of inlet/outlet (X_4)	[50,300]	200	mm
Continuous	Length of counterflow core part (X_5)	[100,1000]	190	mm
Continuous	Width of counterflow core part (X_6)	[100,1000]	357	mm
Continuous	WV transfer resistance (X_7)	[50,300]	78	s/m

d. $50\% \leq MRE \leq 60\%$

where F_1 and F_2 are objective functions. Two objectives in the multi-objective optimisation are to maximise the thermal recovery effectiveness (F_1) modelled in Section 2.1.1 and minimise the PD (F_2) through the MEEs formulated in Section 2.1.3. The design parameters (X_1–X_7) that influence the objective function outputs and constraints (also known as decision variables in an optimisation setting) are given in Fig. 5. Their eligible ranges in this study, and values for the verified design, are presented in Table 2. The multi-objective optimisation was subjected to four linear and nonlinear constraints, which are also denoted in Fig. 5. The first constraint ($0 < \alpha^* < 1$) represents the eligible range for the aspect ratio of the rectangular channel. As the expensive dimension, the maximum membrane area was limited to a specific size (5 m^2 in this study) for the optimisation. The effects of membrane area on the optimisation results were explored by increasing the membrane areas. The third constraint, $X_6/2 < X_4$, sustained the presence of the header part for the quasi-counterflow MEE. The MRE was restricted to 50–60% to ensure the designated indoor humidity levels, as addressed in Section 2.2. A constant airflow rate of 200 m^3/h was used for a single-family house.

The initial population was generated randomly with a size of 2500. The GA solver (gamultiobj) used in MATLAB created a population that was feasible with respect to the bounds of the decision variables and the linear constraints, although this was not necessarily feasible concerning the nonlinear constraints [37]. Only feasible solutions that met all the constraints were kept. Using the fitness of the individuals in the current generation, the algorithm calculated the next generation of the population. At each iteration, the algorithm evaluated the fitness of each solution relative to the objectives. Following this, the non-dominated solutions were selected to form the next generation. The genetic operators were applied to the selected solutions to produce new offspring, which were sequentially evaluated and added to the population. Selection, crossover and mutation were repeated for a set number of generations or until the stopping criteria were met.

For the multi-objective optimisation problem, three stopping criteria were used for the GA solver to specify when to stop. These were: 1) the maximum number of generations exceeded (1500 for this study); 2) the geometric average of the relative change in the spread was exceeding the specified tolerance (0.35 for this study); and 3) no feasible solution was found.

2.4. Experiment setup and measurement uncertainty

The thermal effectiveness, MRE and PD of a quasi-counterflow MEE were experimentally measured in a testing box that complied with the requirements of the EN308 testing standard [39]. The geometries and specifications of the tested MEE are given in Figs. 1 and 3 and Table 1. The test box, including the airflow connections and MEE, is illustrated in

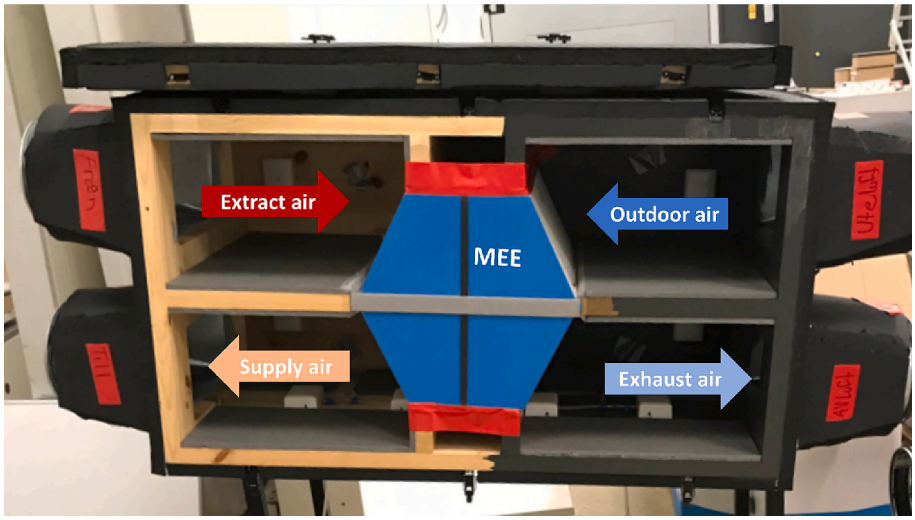

Fig. 6. Test box including the sensors and the quasi-counterflow MEE that complied with the EN308 testing standard.

Table 3
Technical characteristics of the measuring instruments.

Measured parameter	Instrument type and/or model	Instrument accuracy	Instrument measuring range
Temperature	Thermocouple, Type K.	± 1.5%	−40 °C–1000 °C
RH	KIMO TM210	± 3%	5% – 95%
Pressure	KIMO CP113	± 1.5%	± 250 Pa
Airflow rate	Differential pressure transmitter and orifice plate, KIMO CP212	± 0.5%	± 500 Pa

Fig. 6. The sensors for measuring temperature, relative humidity and pressure were placed inside the void space close to the inlets and outlets of the MEE. The temperature, humidity and pressure at each inlet and outlet were measured for different airflow rates (which ranged from 50 to 500 m^3/h) under prescribed dry conditions, based on the EN308 testing standard [39]. The dry bulb temperature of the extract air was 25 °C and the outdoor air was 5 °C. The RH of the extract air was below 30%. The airflow rates were calculated based on the measured pressure difference before and after the orifice plates, based on the standard ISO 5167–1:2003 [40]. The balanced mass airflows were constant for the supply and exhaust sides during the measurements.

The measurement uncertainty was determined by

$$U_r = \sqrt{\left[\left(\frac{\partial Y}{\partial X_1}U_{X_1}\right)^2 + \left(\frac{\partial Y}{\partial X_2}U_{X_2}\right)^2 + \cdots + \left(\frac{\partial Y}{\partial X_i}U_{X_i}\right)^2\right]} \quad (15)$$

where U_{x_i} is the total uncertainty of the variable in question, which consists of bias (B) and precision (P) error. U_{x_i} can be decided by

$$U_{x_i} = \sqrt{B^2 + P^2} \quad (16)$$

The technical characteristics of the used measuring instruments

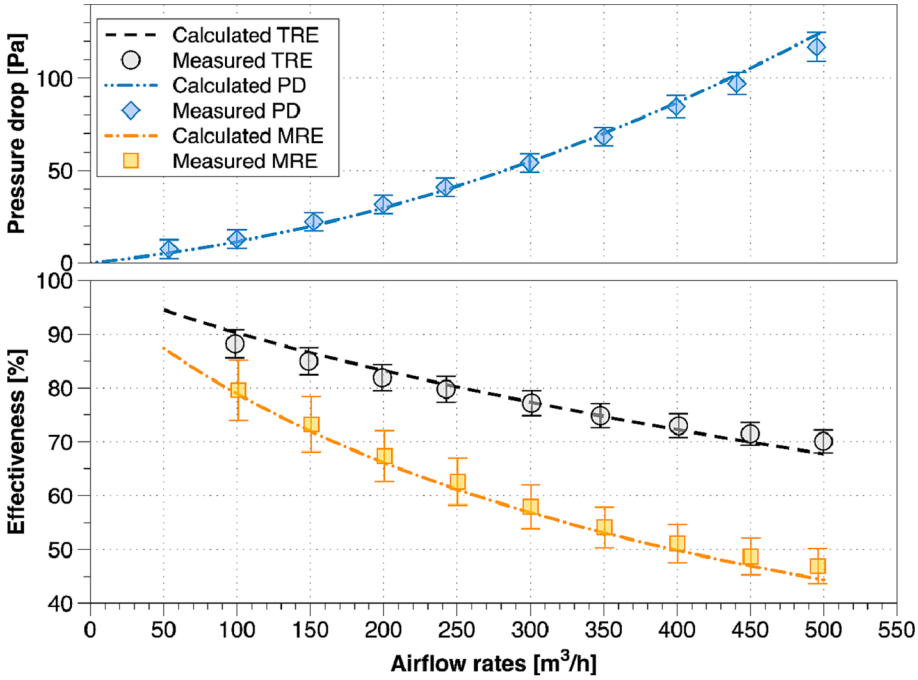

Fig. 7. Validation of analytical MEE models against experimental measurements.

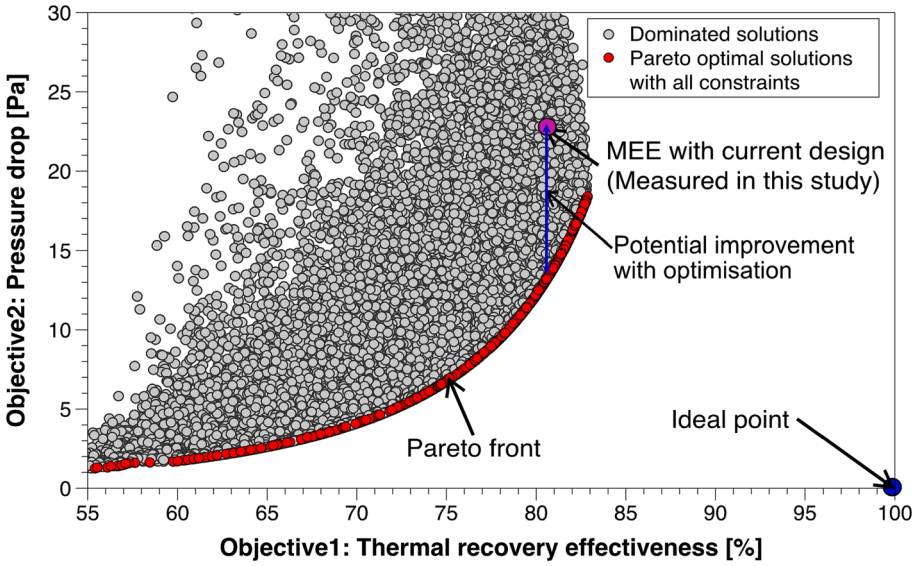

Fig. 8. Dominated and non-dominated (Pareto front) optimal solutions for quasi-counterflow MEE designs.

including instrument type or model, accuracy and measuring range are presented in Table 3.

3. Results and discussion

In this section, the validation of the analytical models is introduced for the thermal effectiveness, MRE and PD of the MEE against the experimental measurements under different airflow rates. The Pareto front, considering the optimisation of the TRE and PD subjecting to the designated constraints, was obtained using the methods described in Section 2.3.

3.1. Validation of analytical models for the membrane energy exchanger

The analytical models proposed for quasi-counterflow MEEs in Section 2.1 were used to calculate the TRE, MRE and PD for the specific MEE illustrated in Figs. 1 and 3 and described in Table 2. The results from the calculations are presented along with the experimental measurements, in Fig. 7. The points in Fig. 7 represent the measurements and uncertainties with 95% of the confidence interval, as addressed in Section 2.4. The analytical calculations are indicated by the lines in Fig. 7. It can be seen from Fig. 7 that there was good agreement between the calculations and the measurements.

Fig. 7 shows opposite trends for PD and recovery effectiveness with increasing airflow rate. These trends are consistent with the heat and mass transfer theories and fluid dynamics addressed in Section 2.1, and also with the experimental data for the quasi-counterflow MEE presented by Liu et al. [14]. High TRE and MRE could be obtained at low airflow rates. The corresponding PD was also relatively low at low airflow rates. However, the effectiveness declined and the PD rose dramatically when the airflow rates increased. In residential buildings, demand-controlled ventilation (DCV) with varying airflows is not typically used and the airflow rates are normally constant even when the residential building is not occupied. Therefore, the optimisation can be performed for the most frequently used airflow rate.

It can be seen from Fig. 7 that the MRE was always lower than the TRE. This can be explained by the fact that the diffusive resistance to moisture transfer through membranes accounts for a large fraction of the total resistance, whereas the conductive resistance in heat transfer through membranes is negligible due to the membrane's thinness. The desired MRE, which was 50–60%, was only achieved when the airflow rates were in the range of 270–400 m^3/h. The TRE for this range of airflow rates was below 80%. This demonstrates the difficulty of providing high TRE, for the tested MEE, when meeting the MRE requirements. These findings suggest that multi-objective optimisation that restricts moisture recovery as a constraint is essential to achieving optimal designs for enhancing thermal performance, reducing pressure drop, and ensuring safe indoor humidity levels.

3.2. Multi-objective optimisation results

The proposed optimisation framework, incorporating the analytical MEE models, was implemented in MATLAB, using a computer configured with an Intel(R) Core i7-8650U CPU at 1.90 GHz and with 16 GB of RAM. With parallel computing, the computation time was approximately 30 min. Fig. 8 presents the dominated solutions and Pareto front (non-dominated solutions), optimising two objective functions and meeting the four previously defined constraints. It can be seen from Fig. 8 that most of the population was distributed close to the Pareto front. This can be explained by the GA working principle for multi-objective optimisation, wherein new generations of a population migrate to a position where better fitness values are obtained in order to find the Pareto front.

All the solutions on the Pareto front in Fig. 8 are optimal non-dominated solutions with no other information provided. It is clear that TRE and PD are competing objectives because one is only improved by degrading the other. The ideal solution, with 100% of TRE and 0 Pa of PD, is located in the bottom right in Fig. 8. With the restrictions on total maximum membrane area (5 m^2) and an MRE of 50–60%, the highest TRE of the MEEs from the multi-objective optimisation was approximately 82% at the operating airflow rate of 200 m^3/h. The PD directly affects the fan power, and thus the electricity consumption and peak power demand. From Fig. 8, it is also apparent that the PD increased dramatically when the TRE increased from 80% to 82%.

The TRE and PD of the MEE with the design measured and shown in Fig. 7 are compared with the Pareto optimal solutions in Fig. 8., The experimentally tested MEE is not located on the Pareto optimal solutions in Fig. 8 and it is one of the dominated solutions in the course of optimisation. The blue line in Fig. 8 shows the potential improvement of the current design using the multi-objective optimisation with respect to pressure penalty. Implementing the optimal design obtained from the multi-objective results, the pressure drop of the tested MEE can be reduced from 22 Pa to 13 Pa (about 41% of reduction) while the TRE is maintained at 80%. The result also indicates that the fan power can be potentially diminished by 41% as the fan power is proportionally linked to the pressure drops through the heat recoveries. Thus, this example

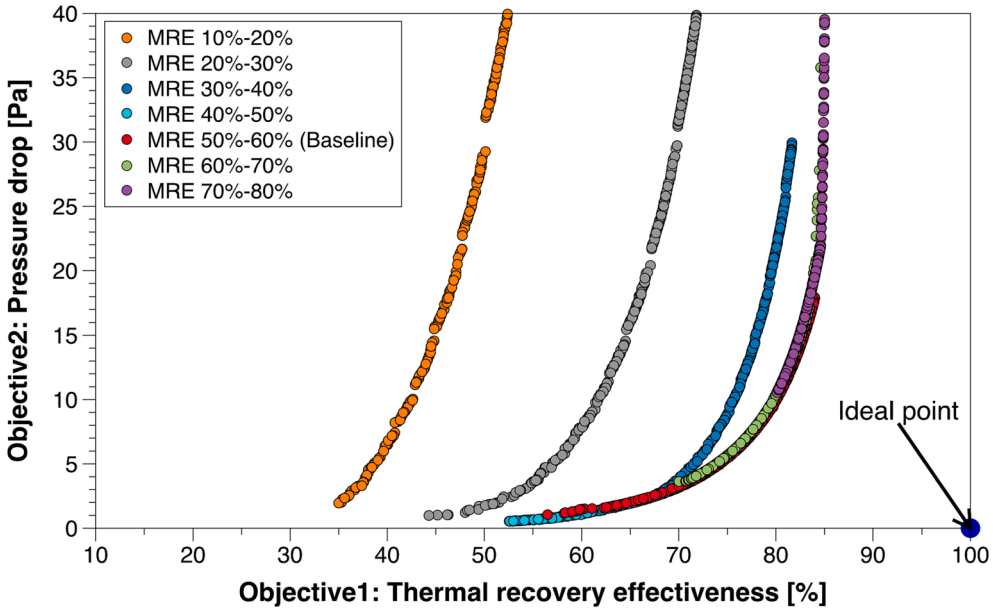

Fig. 9. Pareto fronts for optimisation constraints with different moisture recovery effectiveness.

confirms that the developed multi-objective optimisation design framework can improve the MEE design to facilitate energy use reduction.

The Pareto front provides a set of optimal solutions that allow one to make a decision concerning the preferred design based on demands or requirements. For instance, the optimal solution on the far left in Fig. 8 can achieve 72% of heat recovery effectiveness with a pressure drop lower than 5 Pa.

An extraordinarily low pressure penalty may allow the possibility of utilising heat and moisture recovery for natural and hybrid ventilation, which are very sensitive to PD. The selected Pareto optimal solutions and the values of their corresponding decision variables and other important values can be found in Appendix Table A1. It should be noted that the requirement for the MRE (50–60%) was met for all the Pareto optimal solutions shown in Fig. 8. This was achieved by changing the construction of the MEE and the membranes (WV transfer resistance of the membrane).

As mentioned before, the intention behind constraining an MRE within 50–60% was to improve the indoor too-dry air and not impose a too-humid air problem for the designated single-family house in Oslo, Norway. Different thresholds of MRE can be used for different climates, indoor moisture generation scenarios and ventilation. The determination and explanations of the MRE limits can be found in Liu et al. [16].

The Pareto fronts with different MRE limits were explored using the above procedure and the results are shown in Fig. 9. When the MRE constraint was increased from 10% to 80% in the optimisation, the Pareto fronts moved towards the ideal solution. The maximum TRE increased from 52% to 85%. The reason is that the TRE and MRE are likely to be proportionally coupled, as indicated by the heat and mass transfer analogy. As a result, the maximum TRE is limited to a lower value when the MRE is restricted to a low range, for example, 10–20%. When the constraint range of MRE reaches 40–50% or higher, the

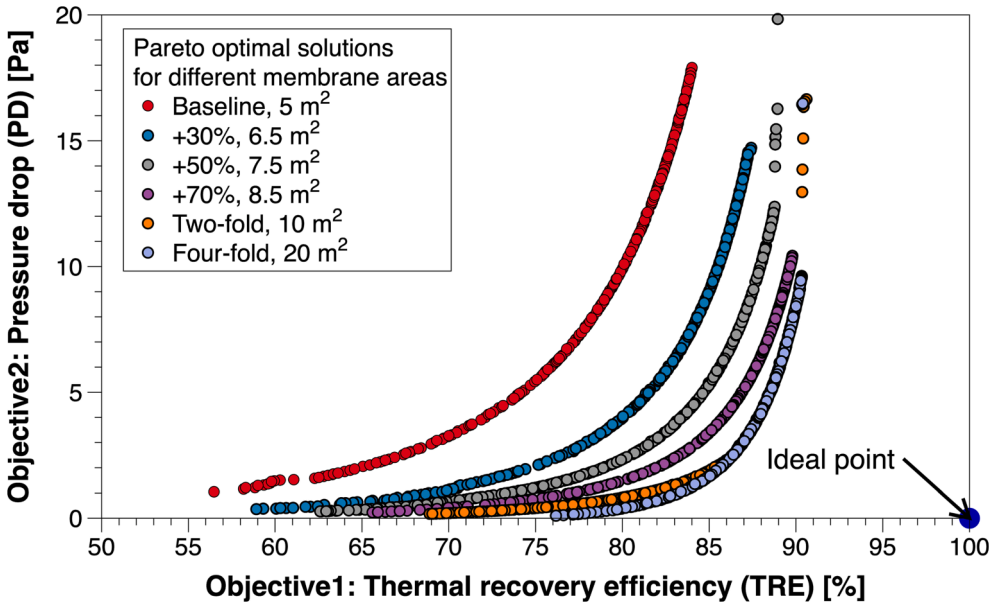

Fig. 10. Pareto fronts for various total membrane areas.

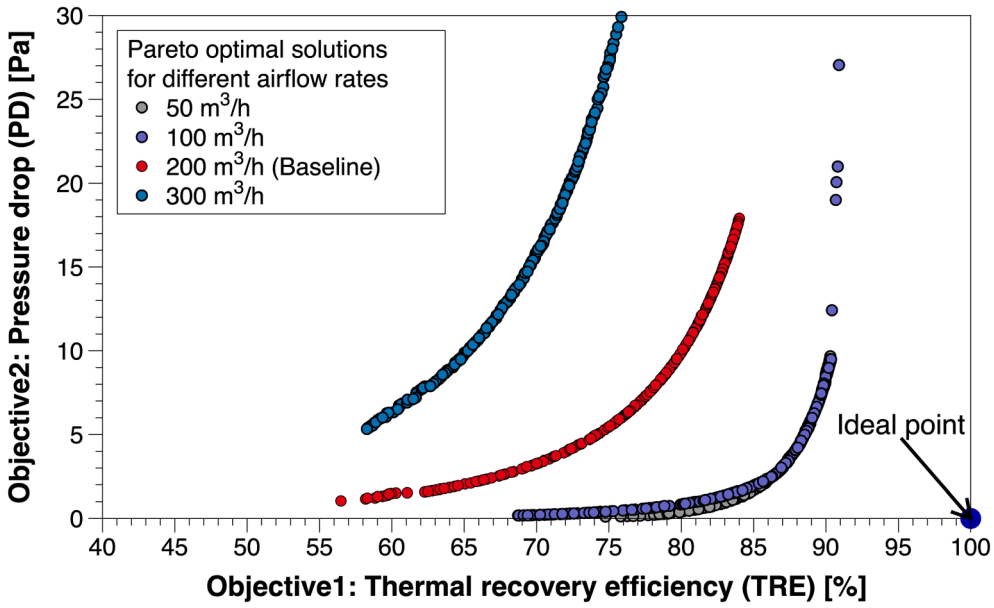

Fig. 11. Pareto fronts for different airflow rates.

maximum TRE obtained from the optimisation is limited to 85%. Therefore, it suggests that the maximum TRE is no longer constrained by the constraint of MRE. However, the total membrane area where heat and mass transfer occur may play a more important role in determining the maximum TRE. Thus, it is important to include the MRE limit as a constraint when indoor moisture levels are considered. Otherwise, the optimised MEE may lead to problematic indoor environments with too-high humidity.

The total membrane area was limited to a maximum value of 5 m^2 in the optimisation, as shown in Fig. 10, to control the cost of the design. Consequently, the maximum TRE in the optimisation was approximately 82%. To explore the influence of the maximum total membrane area on the optimal solutions, the constraint of the maximum total membrane area was changed in the multi-objective optimisation. Compared to the baseline case (5 m^2), enlarging the membrane areas could further increase the maximum TRE from 82% up to 90% with even lower PD (from 22 to 9 Pa), when four-fold membranes were used, as shown in Fig. 10. Overall, increasing the membrane area moved the Pareto front towards the ideal solution. Thus, a better MEE performance could be realised with more membranes. It could also be seen that further improvements in the Pareto optimal results were not obvious when the membrane area was enlarged by 50%, especially for the high TRE. Accordingly, it may not be worth to further improving the TRE and PD by adding more membranes (after increasing the total membrane area by 50%) from a cost-effectiveness perspective. In addition to the higher cost of the increased membrane area, a possibly enlarged volume for the MEE may also need to be considered.

In practice, the MEE operates under different airflow rates for different households. Fig. 11 shows the effects of the operating airflow rates on the Pareto fronts. With decreasing airflow rates, the optimal MEE design solutions are further improved towards the ideal point for the reduced airflow rates. This trend is expected as the TRE increases for low airflow rate due to boosted number of heat transfer units and PD proportionally decreases with reduced airflow rates. For the Pareto front results at low airflow rates (50 m^3/h and 100 m^3/h), their optimal solutions almost overlap with each other and a further reduction in airflow rates will not significantly change the Pareto front. The optimisation results for the MEE design are sensitive to airflow rates in a range of 100 m^3/h to 300 m^3/h.

3.3. Limitations of this study

Moisture recovery is the unique feature of MEEs that distinguish them from sensible-heat-only exchangers. The impact of moisture recovery intensity on indoor humidity levels was considered in the constraints for the multi-objective optimisation framework. The applied threshold (50–60%) of MRE in the current study was derived from a specific single-family house in Oslo, Norway during the heating season [16]. Different MRE thresholds can be calculated and restricted in the optimisation, based on customised demands, different seasons and moisture generation schemes, using the methods presented by Liu et al. [16]. The robustness of the optimal solutions requires further evaluation for different households and moisture generation intensities.

This study emphasized the establishment of a multi-objective optimization framework and demonstrated the feasibility of using the developed methods to improve the performance of membrane energy exchangers. MEE with a rectangular channel was modelled, verified and optimised. For other shapes of channels, the respective numerical models can be incorporated with the developed methods in this study to obtain their optimal results. Another limitation of this study was that the total volume and dimensions of the MEE were not constrained. The dimensions of the MEE could be important in considering the limited space in air handling units.

4. Conclusions

A multi-objective optimisation MEE design framework was developed. The multi-objective optimisation was incorporated with MEE analytical models for heat and mass transfer and PD through MEEs. The analytical models for the quasi-counterflow MEE were verified against experimental measurements. Acceptable agreements between the analytical calculations and experimental measurements were obtained in terms of TRE, MRE and PD. The thermal (TRE) and mechanical (PD) performances were used as two competing objectives to be optimised. The influencing factors for the multi-objective optimisation of membrane energy exchangers were investigated. The main conclusions are as follows:

1. Using the developed multi-objective optimisation, the pressure drops of the measured MEE used for numerical model verification can be further reduced by 41% with thermal recovery effectiveness

Table A1
Decision variables and objective function values for selected Pareto front solutions.

ID	Decision variables for multi-objective optimisation							Function values	
	X_1	X_2	X_3 (mm)	X_4 (mm)	X_5 (mm)	X_6 (mm)	X_7 (mm)	TRE (%)	PD (Pa)
1	46	12	2.1	190.8	327.7	225.6	143.3	84.1	39.6
2	45	12	2.1	191.1	339.6	224.8	140.7	84.1	41.5
3	58	11	4.3	196.2	243.2	210.5	74.8	70.9	4.6
4	46	12	2.1	190.9	325.4	226.6	141.5	84.0	39.0
5	39	12	2.1	190.2	344.4	265.0	147.6	84.2	49.3
6	32	11	2.1	188.6	446.2	267.8	175.7	84.3	72.6
7	46	12	2.1	190.9	326.0	226.0	141.7	84.0	39.3
8	46	12	2.1	190.9	325.2	226.6	141.6	84.0	39.0
9	56	14	8.0	194.8	255.0	211.1	65.3	59.1	1.3
10	50	12	2.1	191.2	294.8	221.8	172.0	83.9	33.3
11	48	12	2.1	191.2	310.2	223.1	142.4	84.0	36.2
12	57	11	6.0	195.3	250.2	211.7	63.2	63.6	2.3
13	34	13	2.1	190.0	377.0	296.4	159.7	84.3	60.6
14	50	12	2.1	191.2	294.8	221.8	172.0	83.9	33.3
15	57	11	3.3	195.7	248.0	212.4	119.3	76.4	8.8
16	56	14	7.0	195.3	253.0	213.8	89.0	61.0	1.7
17	57	12	6.5	194.7	249.6	212.5	88.5	62.0	2.0
18	56	14	8.1	195.1	252.7	210.7	64.7	58.7	1.3
19	39	12	2.1	190.0	349.0	263.8	145.0	84.2	49.9
20	56	11	2.2	195.2	252.1	214.0	168.9	83.3	24.0
21	56	14	7.8	195.0	256.3	211.6	72.8	59.4	1.4
22	57	11	2.7	194.7	243.4	215.4	131.7	80.2	14.3
23	34	13	2.1	190.0	377.0	296.4	159.7	84.3	60.6
24	46	12	2.1	190.8	327.5	225.6	143.6	84.1	39.6
25	50	12	2.1	191.6	299.6	218.9	169.3	84.0	33.9
26	57	11	5.9	195.0	249.4	212.2	120.8	63.7	2.3
27	56	14	8.0	194.9	254.1	210.9	65.0	58.9	1.3
28	56	14	8.0	194.8	255.0	211.1	65.3	59.1	1.3
29	57	11	5.7	195.5	246.5	213.7	86.3	64.5	2.5
30	57	11	5.2	195.5	246.0	213.8	77.7	66.7	3.1
31	57	11	5.0	195.6	247.8	212.6	101.4	67.6	3.4
32	58	11	4.4	195.5	244.6	210.1	127.3	70.3	4.4
33	42	12	2.1	193.4	363.6	228.0	154.2	84.1	45.8
34	57	11	3.1	195.9	244.7	214.1	129.8	77.8	10.4

unchanged. This finding confirms that the multi-objective optimisation can be applied to provide a set of optimal solutions considering both thermal recovery effectiveness and pressure drop with fulfilling constraints of total membrane area and recommended moisture recovery effectiveness.

2. The MEE designs with pressure drop lower than 5 Pa and heat recovery effectiveness higher than 70% have been identified from the obtained Pareto optimal solutions. The optimal designs with extraordinarily low pressure penalty may enable the use of heat recovery in natural or hybrid ventilation.
3. The Pareto fronts are influenced by the moisture recovery effectiveness in constraints, total membrane areas and operating airflow rates. Increasing membrane areas fourfold from a baseline of 5 m^2 to its fourfold of 20 m^2 had the result of increasing the maximum thermal recovery effectiveness by 7% (from 83% to 90%). The cost-effective design can be obtained from the Pareto fronts for different moisture recovery effectiveness, membrane areas, and operating airflow rates.

This study has facilitated a better understanding of the optimal design and ways of improving the performance of membrane energy exchangers, offering significant potential in contributing to energy-efficient and cost-effective ventilation.

CRediT authorship contribution statement

Peng Liu: Conceptualization, Methodology, Data curation, Validation, Visualization, Writing – original draft, Software. **Hans Martin Mathisen:** Methodology, Writing – review & editing. **Maria Justo Alonso:** Methodology, Writing – review & editing. **Anneli Halfvardsson:** Validation, Writing – review & editing.

Declaration of Competing Interest

The authors declare that they have no known competing financial interests or personal relationships that could have appeared to influence the work reported in this paper.

Data availability

Data will be made available on request.

Acknowledgements

This research was funded by the Research Council of Norway (NFR) and Flexit AS through the Defreeze MEE Now project (NFR grant number: 296489). The authors thank Lars Wessman at the laboratory of Flexit for performing the experimental measurements. Fredrik Karlsson from Flexit and Luis Caetano from SINTEF Community are gratefully acknowledged for their comments and inputs on the optimisation.

Appendix

Table A1.

References

[1] IEA – International Energy Agency. IEA n.d. https://www.iea.org/data-and-statistics (accessed January 2, 2023).
[2] Energy Technology Perspectives 2017 - Catalysing Energy Technology Transformations n.d. 10.1787/ENERGY_TECH-2017-EN.
[3] Kusiak A, Xu G, Zhang Z. Minimization of energy consumption in HVAC systems with data-driven models and an interior-point method. Energ Conver Manage 2014;85:146–53. https://doi.org/10.1016/j.enconman.2014.05.053.

[4] Ürge-Vorsatz D, Cabeza LF, Serrano S, Barreneche C, Petrichenko K. Heating and cooling energy trends and drivers in buildings. Renew Sustain Energy Rev 2015;41:85–98. https://doi.org/10.1016/j.rser.2014.08.039.
[5] Luo Y, Cheng N, Zhang S, Tian Z, Xu G, Yang X, et al. Comprehensive energy, economic, environmental assessment of a building integrated photovoltaic-thermoelectric system with battery storage for net zero energy building. Build Simul 2022;15:1923–41. https://doi.org/10.1007/s12273-022-0904-1.
[6] Picallo-Perez A, Sala-Lizarraga JM, Odriozola-Maritorena M, Hidalgo-Betanzos JM, Gomez-Arriaran I. Ventilation of buildings with heat recovery systems: thorough energy and exergy analysis for indoor thermal wellness. J. Build. Eng. 2021:39.
[7] Albdoor AK, Ma Z, Al-Ghazzawi F, Arıcı M. Study on recent progress and advances in air-to-air membrane enthalpy exchangers: materials selection, performance improvement, design optimisation and effects of operating conditions. Renew Sustain Energy Rev 2022;156:111941. https://doi.org/10.1016/J.RSER.2021.111941.
[8] Li J, Shao S, Wang Z, Xie G, Wang Q, Xu Z, et al. A review of air-to-air membrane energy recovery technology for building ventilation. Energ Buildings 2022;265:112097. https://doi.org/10.1016/J.ENBUILD.2022.112097.
[9] Zhang LZ, Niu JL. Energy requirements for conditioning fresh air and the long-term savings with a membrane-based energy recovery ventilator in Hong Kong. Energy 2001;26:119–35. https://doi.org/10.1016/S0360-5442(00)00064-5.
[10] Liu P, Nasr MR, Ge G, Alonso MJ, Mathisen HM, Fathieh F, et al. A theoretical model to predict frosting limits in cross-flow air-to-air flat plate heat/energy exchangers. Energ Buildings 2015;110:404–14. https://doi.org/10.1016/j.enbuild.2015.11.007.
[11] Bai HY, Liu P, Justo Alonso M, Mathisen HM. A review of heat recovery technologies and their frost control for residential building ventilation in cold climate regions. Renew Sustain Energy Rev 2022;162:112417. https://doi.org/10.1016/J.RSER.2022.112417.
[12] Huizing R, Chen H, Wong F. Contaminant transport in membrane based energy recovery ventilators. Sci Technol Built Environ 2015;21:54–66. https://doi.org/10.1080/10789669.2014.969171.
[13] Liu P, Mathisen HM, Skaten M, Justo AM. Use of membrane energy exchanger in ventilation: Odour sensory measurement. Build Environ 2022;222:109430. https://doi.org/10.1016/j.buildenv.2022.109430.
[14] Liu P, Justo Alonso M, Mathisen HM, Simonson C. Performance of a quasi-counter-flow air-to-air membrane energy exchanger in cold climates. Energ Buildings 2016;119:129–42. https://doi.org/10.1016/j.enbuild.2016.03.010.
[15] Zhang L-Z. Progress on heat and moisture recovery with membranes: from fundamentals to engineering applications. Energ Conver Manage 2012;63:173–95. https://doi.org/10.1016/j.enconman.2011.11.033.
[16] Liu P, Justo Alonso M, Mathisen HM, Halfvardsson A, Simonson C. Understanding the role of moisture recovery in indoor humidity: an analytical study for a Norwegian single-family house during heating season. Build Environ 2023;229:109940. https://doi.org/10.1016/j.buildenv.2022.109940.
[17] Justo Alonso M, Liu P, Mathisen HM, Ge G, Simonson C. Review of heat/energy recovery exchangers for use in ZEBs in cold climate countries. Build Environ 2015;84:228–37. https://doi.org/10.1016/j.buildenv.2014.11.014.
[18] Liu P, Mathisen HM, Justo Alonso M, Simonson C. A frosting limit model of air-to-air quasi-counter-flow membrane energy exchanger for use in cold climates. Appl Therm Eng 2017:111. https://doi.org/10.1016/j.applthermaleng.2016.10.010.
[19] Zhang L-Z. Heat and mass transfer in a quasi-counter flow membrane-based total heat exchanger. Int J Heat Mass Transf 2010;53:5478–86. https://doi.org/10.1016/j.ijheatmasstransfer.2010.07.009.
[20] Kays WM, London AL. Compact heat exchangers. Krieger Publishing Company; 1984.
[21] Al-Waked R, Nasif MS, Mostafa DB. Enhancing the performance of energy recovery ventilators. Energ Conver Manage 2018;171:196–210. https://doi.org/10.1016/j.enconman.2018.05.105.
[22] Asasian-Kolur N, Sharifian S, Haddadi B, Pourhosseinian M, Mousazadeh Shekarbaghani Z, Harasek M. Membrane-based enthalpy exchangers for coincident sensible and latent heat recovery. Energ Conver Manage 2022;253:115144. https://doi.org/10.1016/J.ENCONMAN.2021.115144.
[23] Niroomand S, Fauchoux MT, Simonson CJ. The mechanisms of frost formation on a semipermeable membrane. Int J Heat Mass Transf 2022;182:121912. https://doi.org/10.1016/j.ijheatmasstransfer.2021.121912.
[24] Liu P, Justo Alonso M, Mathisen HM, Halfvardsson A. The use of machine learning to determine moisture recovery in a heat wheel and its impact on indoor moisture. Build Environ 2022;215:108971. https://doi.org/10.1016/J.BUILDENV.2022.108971.
[25] Koester S, Klasen A, Lölsberg J, Wessling M. Spacer enhanced heat and mass transfer in membrane-based enthalpy exchangers. J Membr Sci 2016;520:566–73. https://doi.org/10.1016/j.memsci.2016.06.002.
[26] Woods J, Kozubal E. Heat transfer and pressure drop in spacer-filled channels for membrane energy recovery ventilators. Appl Therm Eng 2013;50:868–76. https://doi.org/10.1016/j.applthermaleng.2012.06.052.
[27] Shah RK, Sekulic DP. Fundamentals of heat exchanger design. John Wiley & Sons; 2003.
[28] Roulet C -a, Heidt FD, Foradini F, Pibiri M-C. Real heat recovery with air handling units. Energy and Buildings 2001;33:495–502. 10.1016/S0378-7788(00)00104-3.
[29] Konak A, Coit DW, Smith AE. Multi-objective optimization using genetic algorithms: a tutorial. Reliab Eng Syst Saf 2006;91:992–1007. https://doi.org/10.1016/j.ress.2005.11.018.
[30] Liu P, Justo Alonso M, Mathisen HM, Simonson C. Energy transfer and energy saving potentials of air-to-air membrane energy exchanger for ventilation in cold climates. Energ Buildings 2017;135:95–108. https://doi.org/10.1016/j.enbuild.2016.11.047.
[31] Niu JL, Zhang LZ. Membrane-based Enthalpy Exchanger: material considerations and clarification of moisture resistance. J Membr Sci 2001;189:179–91. https://doi.org/10.1016/S0376-7388(00)00680-3.
[32] Kays W, Crawford M, Weigand B. Convective heat & mass transfer w/ engineering subscription card. Incorporated: McGraw-Hill Companies; 2005.
[33] Min J, Su M. Performance analysis of a membrane-based enthalpy exchanger: effects of the membrane properties on the exchanger performance. J Membr Sci 2010;348:376–82. https://doi.org/10.1016/j.memsci.2009.11.032.
[34] Pignotti A, Shah RK. Effectiveness-number of transfer units relationships for heat exchanger complex flow arrangements. Int J Heat Mass Transf 1992;35:1275–91. https://doi.org/10.1016/0017-9310(92)90184-T.
[35] Liu P, Justo Alonso M, Mathisen HM, Halfvardsson A. Development and optimization of highly efficient heat recoveries for low carbon residential buildings. Energ Buildings 2022;268:112236. https://doi.org/10.1016/J.ENBUILD.2022.112236.
[36] Mitchell M. An introduction to genetic algorithms. MIT Press; 1998.
[37] Find Pareto front of multiple fitness functions using genetic algorithm - MATLAB gamultiobj - MathWorks Nordic n.d. https://se.mathworks.com/help/gads/gamultiobj.html (accessed December 29, 2022).
[38] Multi-Objective Optimization using Evolutionary Algorithms | Wiley n.d. https://www.wiley.com/en-us/Multi+Objective+Optimization+using+Evolutionary+Algorithms-p-9780471873396 (accessed December 29, 2022).
[39] BS EN 308:1997 - Heat exchangers. Test procedures for establishing the performance of air to air and flue gases heat recovery devices.
[40] ISO 5167-1. Measurement of fluid flow by means of pressure differential devices - Part 1: Orifice plates, nozzles and Venturi tubes inserted in circular cross-section conduits running full, International Standards Organization, Geneva, Switzerland.; 2003.